LAWRENCE
LIVERMORE
NATIONAL
LABORATORY

LLNL-TR-675956

Radiation Background and Attenuation Model Validation and Development

D. E. Peplow, C. Santiago

August 5, 2015

Disclaimer

This work performed under the auspices of the U.S. Department of Energy by Lawrence Livermore National Laboratory under Contract DE-AC52-07NA27344.

Radiation Background and Attenuation Model Validation and Development

Project Report for

Tool to Improve Urban Search Planning

LL14-V-Urban Search Planning Tool-PD3RS

LLNL-TR-675956

Douglas E. Peplow
Oak Ridge National Laboratory

and

Claudio P. Santiago
Lawrence Livermore National Laboratory

July 2015

This work was performed under the auspices of the U.S. Department of Energy by Lawrence Livermore National Laboratory under Contract DE-AC52-07NA27344.

Executive Summary

This report describes the initial results of a study being conducted as part of the Urban Search Planning Tool project. The study is comparing the Urban Scene Simulator (USS), a one-dimensional (1D) radiation transport model developed at LLNL, with the three-dimensional (3D) radiation transport model from ORNL using the MCNP, SCALE/ORIGEN and SCALE/MAVRIC simulation codes. In this study, we have analyzed the differences between the two approaches at every step, from source term representation, to estimating flux and detector count rates at a fixed distance from a simple surface (slab), and at points throughout more complex 3D scenes.

First, we compared the sources and the individual source emission spectra from GADRAS (the 1D transport code used by USS) and SCALE/ORIGEN for each of the three isotopes considered. The emission spectra from the sources were found to match quite well.

The next step was to compare the flux at a detector position from a single finite slab computed by the LLNL USS approach with 3D Monte Carlo (MC) estimates at different potential detector locations. Experiments revealed that the LLNL USS approach for estimating the flux at a detector position from a single finite slab is fairly close to the 3D MC simulations. The maximum error for the range of slab sizes and detector distances used in this study was about 15%.

Since the LLNL USS approach ignores scattering, 3D calculations with multiple slabs were performed to quantify the error due to omitting the contribution of scattered photons. By ignoring scatter from slabs close to the detector, the LLNL USS approach under-predicts the low-energy flux arriving at the detector by approximately 30% for energies below 200 keV.

For full scene calculations using the 3D Monte Carlo codes, a two-step process was used in order to model the detector count rates at many locations at once. For the first step, a detector response function for converting a mono-energetic photon flux into an energy-deposited spectra was constructed for the range of possible incident photon energies. MCNP was used to simulate a NaI detector placed inside a hypothetical spherical source. In the second step, the 3D simulation computes the energy-dependent photon flux in every part of the model where a detector could be placed, without actually having the detector model anywhere. The detector count rate at any position is then found by convolving the computed flux spectrum for that location with the detector response function. This methods produces very similar results to explicitly modeling the detector in the full scene but does not take into account the detector orientation, which is a large effect for the 2”×4”×16” NaI detectors commonly used in search operations.

Finally, we performed full scene comparisons using a 6”×6” cylindrical detector since the impact of detector orientation is very small and can be handled by the two-step approach described above. The LLNL USS was used to generate two sets of scenes that differ by the average building heights. Within each set, three scenes were generated varying the proportion of empty lots. These six scenes were then computed with the 3D system, computing photon fluxes everywhere and determining the detector count rates using the detector response function. The background count rates computed by the two transport systems correlate well but differ in magnitude by a factor of about 2. Count rates predicted by the USS are roughly half of the MAVRIC count rates and the cause of this discrepancy is still being investigated.

This page intentionally left blank.

Contents

1 Introduction

The overall mission of the Urban Search Planning Tool project is to develop a computational tool that would create an optimal search plan for a given set of search assets, search area, and threat source(s). Two types of searches are to be considered: 1) a wide-area search in which vehicle mounted detectors are driven over a predefined section of a city to clear areas between the streets and exterior walls of buildings, and 2) a high-interest location search in which human-portable detectors are carried around the perimeter of a building to clear interior spaces to the extent possible. Dwell times spent at locations along the search route must be long enough to show that a threat source of a certain activity is not near that measurement location. These times depend on the estimated signal-to-noise ratio between the threat source and background count rates in parts of the energy spectrum of interest. Direct measurements, when available, can be used to estimate background rates, but in general a model of the search area and a radiation transport tool are required to estimate background and source contributions. Since the radiation transport tool will be called many times for all of the places within the scene where the threat object could be located, the tool must be very fast. This report describes an ongoing study comparing the accuracy and computational burden of two transport models: a fast-running approximate one-dimensional (1D) model and a high-resolution computationally intensive three-dimensional (3D) model.

In preliminary studies [Faissol, 2012], Lawrence Livermore National Laboratory (LLNL) developed the Urban Scene Simulator (USS) utilizing the 1D transport code GADRAS [Mitchell, 1988]. This model involves a scene generation tool which builds a scene that models the ground as well as building walls of different thicknesses made of concrete, brick and granite. This tool can be used to model streets, blocks buildings. Different detector locations may be considered on the streets. Each building in a scene is described by 4 different slabs (surfaces) each having a material, a thickness and the concentration of each isotope of interest. Because of errors in the slab model in earlier versions of GADRAS, spherical sources were modeled in GADRAS for ground (concrete) 20 cm thick and every combination of wall material (brick, concrete, and granite), thickness (5, 7, 9, 11, 13, 15, 17, 19, 21, 23, and 25 cm) and nuclide (^{40}K, ^{232}Th and ^{238}U/^{235}U). The sources consist of the detector response for each material considered with the detector positioned 100 cm from the source. A detailed description of source generation will be given later in this document.

The 1D model computes the background at a given detector location by casting a number of rays from this position in order to estimate the solid angle subtended by each surface. The rays are randomly cast over all possible directions (for a 4π detector) or on a half sphere (for a 2π detector). It was empirically verified that 1000 randomly-generated rays is enough to get a very good approximation for the solid angle subtended by each surface in the scene. The solid angle and the concentration values for each nuclide in each surface are then used to estimate the background. Only surfaces within a given range from the detector are considered. This range is currently set to 100 m. Since slab sources can be accurately modeled in newer versions of GADRAS, the current version of the LLNL USS models sources as slabs. The method for computing the background in the 1D model is shown later in this document.

In parallel to the LLNL approach, Oak Ridge National Laboratory (ORNL) is providing rigorous 3D radiation transport solutions for the same scene models LLNL is using to compute attenuation of signals from a threat source and background count rates. Continuous-energy Monte Carlo calculations with the detector explicitly modeled would provide the most rigorous estimates of count rates, but these calculations would be prohibitive due to the long computation times required for convergence. For the large urban scenes considered in this project, two things can be done to help reduce computational times. First, separating the detector response function from the transport and computing just the energy-dependent flux at all possible detector positions can help reduce the required run time as long as an accurate flux-to-count rate conversion factor can be formulated. Second, applying ORNL's signature

automated variance reduction using deterministic estimates can drastically reduce Monte Carlo computational times focusing the simulation on the particles that will contribute to the desired solution. But even with these two techniques, rigorous three-dimensional calculations will still require orders of magnitude more time than the USS.

Due to the different nature of the transport methods employed, there should be noticeable differences in the solutions obtained from the USS and from 3D Monte Carlo. For attenuation, the USS uses the perpendicular distance through a wall and computes a reduced count rate based on a single exponential (for HEU sources) or a lookup table (for ^{137}Cs sources), which does not really take into account the change in spectral shape of the photon flux when passing through the wall. Buildup and scatter are ignored in threat source calculations. For background calculations, the USS does a simple sum over all of the building faces and roadway segments, treating each as a simple system of a single slab emitter and a detector. This approach does not include the scatter from other building faces and other roadway segments in the scene. Even though there will be differences in estimated threat source count rates and background count rates, the important question is whether the final optimized search plan is sensitive to these differences. By ignoring scatter, the USS should compute lower count rates than the 3D simulations, but if the USS is low across the entire scene, the final search plan may not change considerably.

The faster, lower-fidelity LLNL approaches and slower, higher-fidelity ORNL approaches were compared step-by-step to ensure that the same variables were being modeled in each case. Most of the work in the first year of the project has focused on background calculations for wide-area vehicle-mounted detectors. This report details the different steps used by each approach and how they compare to each other. The report does not try to compare either method to experimental results – that will come after well-controlled measurements are made in a simplified urban setting.

2 Background Source Emission Spectra

As a first step, the sources and the individual source emission spectra from the LLNL USS and the SCALE/ORIGEN code (which will be the source in the 3D Monte Carlo codes) were compared to ensure that the same sources were being modeled. LLNL's initial studies considered five emitters (^{40}K, ^{226}Ra, ^{232}Th, ^{235}U, and ^{238}U) that could all have different concentrations (Bq/kg) in concrete, brick and granite. The two uranium isotopes should always have activities in a ratio defined by their natural abundances and their half-lives, so those can be merged into one source. ^{226}Ra is a daughter of ^{238}U and should be in secular equilibrium. Some measurements have shown this to be the case and other measurements show that the activities are not the same, due to natural processes that allow the different elements in the ^{238}U decay chain to move through rock formations at different rates. For simplicity, both the LLNL USS and the ORNL rigorous modeling will consider three independent sources: ^{40}K, ^{232}Th and all of its daughters in secular equilibrium, and a mixture of ^{235}U and ^{238}U and all of their daughters in secular equilibrium.

Note that after measuring the building and road materials at the Fort Indiantown Gap facility, this approach may be modified to separate the decay chains into several parts and requiring more independent sources. Since building materials are processed (chemically or at high temperature), the different elements in the decay chains could have been removed to different extents, breaking the secular equilibrium assumption.

SCALE/ORIGEN was used to determine the photon spectra emitted by each of the NORM sources. Each was decayed to a long time to ensure that all of the daughters were in secular equilibrium with the parent. (Technically, with the long times used here, this would be called 'transient equilibrium' because parent is

decaying over the time considered. At present day and with the time scales of measurements being very short compared to the parent half-life, 'secular equilibrium' is more commonly used.) **Table 1** displays the data used to determine the starting amounts for each NORM source so that at the final time (present day), the activity of the parent was 1 Bq.

Table 1. Data used to set initial isotope amounts in SCALE/ORIGEN

	^{40}K	Th-232	U-235	U-238	Data Source
atomic mass	40	232	235	238	ORIGEN data
abundance			0.0072	0.992745	Chart of Nuclides
half-life (sec)	3.938400E+16	4.433800E+17	2.221000E+16	1.410000E+17	origen data
decay const (/sec)	1.759972E-17	1.563325E-18	3.120879E-17	4.915937E-18	ln(2)/t-half
mass (g)	3.774013E-06	2.464267E-04		8.039327E-05	for 1 Bq today
mass (g)			5.757121E-07		based on U-238
decay (seconds)	1.410000E+17	1.410000E+17	1.410000E+17	1.410000E+17	age of earth
starting mass (g)	4.513684E-05	3.071982E-04	4.691285E-05	1.607865E-04	

The final emission spectra consist of many lines from all of the daughters and are stored in 1 keV bins from 1 keV to 10 MeV. At the final time (present day), 1 Bq of ^{232}Th includes 1 Bq of ^{228}Th, ^{228}Ac, ^{228}Ra, ^{224}Ra, ^{220}Rn, ^{216}Po, ^{212}Bi, and ^{212}Pb, as well as smaller activities of ^{212}Po and ^{208}Tl. One Bq of ^{238}U includes 1 Bq of ^{234}U, ^{234m}Pa, ^{234}Th, ^{230}Th, ^{226}Ra, ^{222}Rn, ^{218}Po, ^{214}Po, ^{210}Po, ^{214}Bi, ^{210}Bi, ^{214}Pb and ^{201}Pb with smaller activities of ^{234}Pa, ^{218}Rn, ^{218}At, ^{210}Tl, ^{206}Tl and ^{206}Hg. ^{235}U is also included in the uranium mixture, scaled by its current natural abundance. This source then includes 0.0457 Bq of ^{235}U, ^{231}Pa, ^{231}Th, ^{227}Th, ^{227}Ac, ^{223}Ra, ^{219}Rn, ^{215}Po, ^{211}Bi, ^{211}Pb, and ^{207}Tl with small activities of ^{223}Fr and ^{211}Po. Materials found in nature may not be in exact secular equilibrium due to the different mobility of the different daughter elements in whatever matrix the parent is located in. Also, radon is a gas which is very mobile and a significant fraction may escape the matrix, leading to lower levels of its daughters compared to the above lists. Materials that have been processed can be even further from secular equilibrium depending on the degree of chemical separation that took place during production.

Figure 1 shows the comparisons of the ORIGEN emission spectra to the emission spectra taken from GADRAS used by the LLNL USS. In each graph, the spectra from each code system have been collapsed to coarse bin structures for easier comparison.

Overall, the emission spectra match quite well. ORIGEN considers bremsstrahlung from electron decays (noticeable at low energies in the ^{40}K spectrum) and has slightly different line energies for some isotopes in the ^{238}U source compared to GADRAS.

^{40}K
0.1433 photon/sec

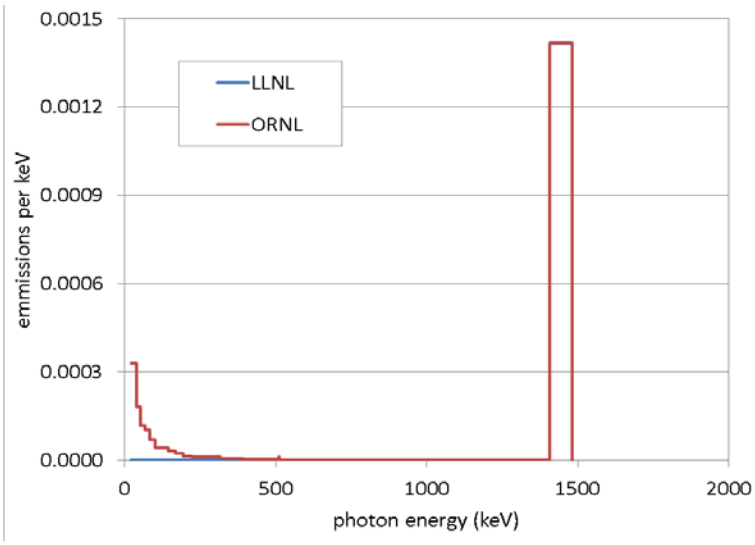

^{232}Th
3.9974
gammas/sec

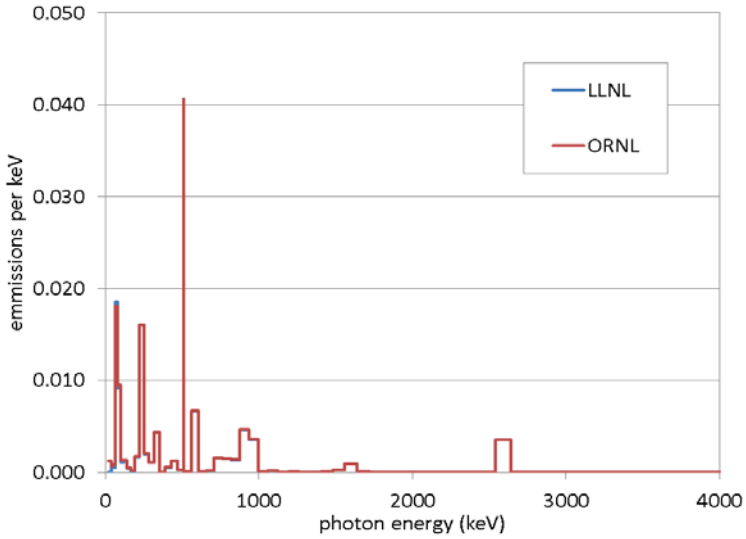

^{238}U/^{235}U
3.4725
gammas/sec

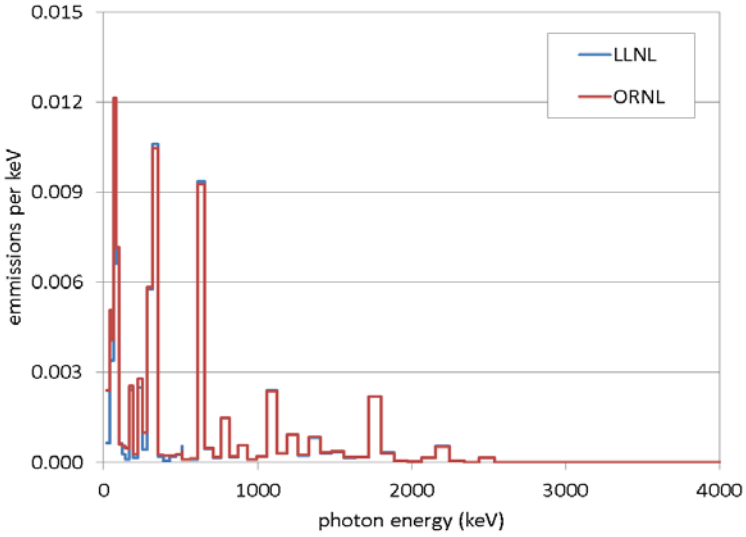

Figure 1. Comparison of LLNL USS and ORNL's SCALE/ORIGEN source emission spectra.

2.1 Leakage Current from an Infinite Slab

The LLNL USS uses GADRAS to precompute the surface leakage flux of every combination of material (brick, concrete, and granite), thickness (5, 7, 9, 11, 13, 15, 17, 19, 21, 23, and 25 cm) and isotope (^{40}K, ^{232}Th and ^{238}U/^{235}U). The leakage flux from each slab source in the model is then combined to determine the background count rate. In their preliminary work, LLNL used spherical models, with radii much larger than the thickness, to approximate slab geometry. This was the only choice in older versions of GADRAS.

In the 3D Monte Carlo codes, the NORM sources are modeled as uniformly distributed throughout a given section of roadway or building wall. This is closer to the real situation and includes edge effects that are not included in the fast/approximate methods. Calculations with both systems were run to ensure that the surface leakage currents leaving the slab were similar.

In the course of the comparisons, several things were learned. First, the GADRAS spherical models with voided centers do not produce the same leakage current as the slab-based models in later versions of GADRAS. It must be remembered that the pie-slice visualization shown in the GADRAS GUI (right) is just a portion of the spherical model. In the 1D transport calculation, the whole sphere is included such that source emissions towards the direction of the center of the sphere could contribute to the current leaving the outer surface on the opposite side of the sphere. For thin slabs, this produces a large over-estimation of the surface leakage current compared to the GADRAS 1D slab models or calculations done with MCNP [LANL, 2003]. Filling the interior with a very dense material prevents photons from crossing the sphere center and leaking out the other side. The drawback of this approach is that photons could still be reflected by this material back out, incorrectly increasing the leakage computed for the outer boundary.

The second important lesson learned is that even though the GADRAS manual says it is computing flux, it is really computing current. This fact was confirmed by the GADRAS developers. Flux and current are physically different quantities and have different magnitudes. Initial comparisons of energy-dependent leakages between SCALE/MAVRIC (flux) and GADRAS (current) were off in both shape and magnitude. Later comparisons of GADRAS and MCNP (which can compute both current and flux) are shown in **Figure 2**. There is good agreement in the surface leakage current values from infinite slabs.

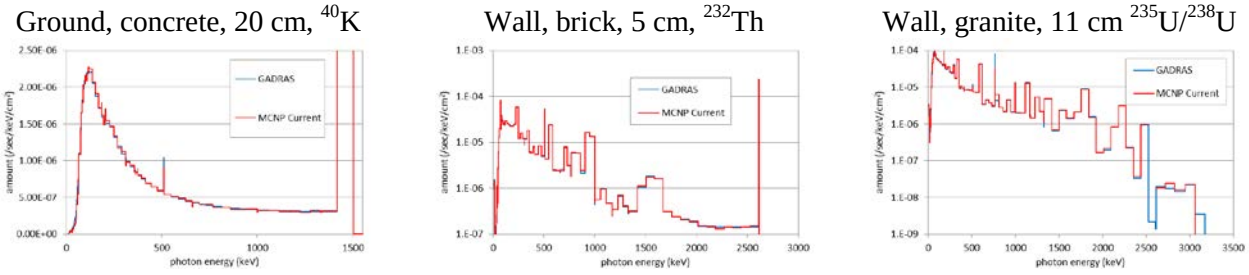

Figure 2. Surface leakage current from an infinite slab computed with GADRAS and MCNP

It should be noted that the GADRAS team was very cooperative in helping the Urban Search team work through some minor bugs and in helping to explain more details about the GADRAS 1D transport.

For its newer 1D slab geometry, GADRAS computes the leakage current from both faces of a finite dimension slab. To obtain the current from a 5 cm thick infinite slab (to reduce edge effects) of brick with an activity concentration of 1 Bq/kg, the values of the activities of the unstable isotopes are computed using:

quantity		units	value
A	activity	Ci	
h	height	cm	10000
w	width	cm	10000
S	surface area	cm^2	$hw = 10^8$
t	thickness	cm	5
V	volume	cm^3	$St = 5\times10^8$
ρ	density	kg/cm^2	0.0018

$$A = (1\ \text{Bq/kg})\ \frac{V\rho}{2S}\ \frac{1\ \text{Ci}}{37\times10^9\ \text{Bq}}$$

$$A = (1\ \text{Bq/kg})\ \frac{t\rho}{2}\ \frac{1\ \text{Ci}}{37\times10^9\ \text{Bq}} = 1.2162\times10^{-13}\ \text{Ci}$$

The activity of ^{235}U is equal to $A_{238}\ (\lambda_5/\lambda_8)\ 0.0072 = 0.04571\ A_{238}$.

The final GADRAS input file for a 5 cm thickness of brick with a ^{238}U/^{235}U source is then:

```
Version: 18.4.3
2   0.000
!

brick
2.500E+00 1.800E+00 4.500E+09 0.000E+00 0.000E+00 0.000E+00 F 0  5  3
          0.000E+00 0.000E+00 0.000E+00 0.000E+00 2 1.000E+04 1.000E+04
  O         Al        Si        Ca        Fe
       8000     13000     14000     20000     26000
  5.250E+01 5.000E-01 4.490E+01 1.400E+00 7.000E-01
  0.000E+00 0.000E+00 0.000E+00 0.000E+00 0.000E+00
  U234      U235      U238
      92234     92235     92238
  -1.22E-13 -5.60E-15 -1.22E-13
  0.000E+00 0.000E+00 0.000E+00
  0.000E+00 0.000E+00 0.000E+00
  0.000E+00 0.000E+00 0.000E+00
  0.000E+00 0.000E+00 0.000E+00
!
```

3 Flux at Point from a Finite Slab

For a rectangular slab with its top surface center at the origin and aligned with the $\hat{x}$- and $\hat{y}$-axes with:

A	length of slab in $\hat{x}$ direction
B	width of slab in $\hat{y}$ direction
D	detector position (x_D, y_D, z_D) and
$j(\mu)$	Uniform surface leakage current per unit area with $\int_0^1 j(\mu)d\mu = j_0$,

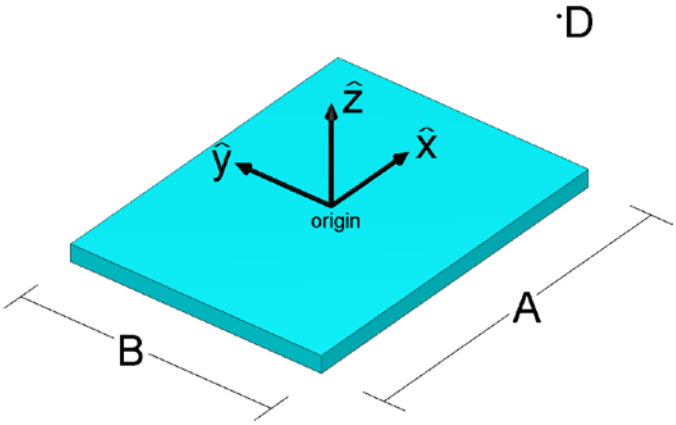

the flux ϕ at the detector position D can be found by integrating the leakage current directed at the detector over the surface of the slab as

$$\phi = \int_{-B/2}^{+B/2} \int_{-A/2}^{A/2} \frac{j(\mu)}{4\pi\, r^2}\, dx\, dy$$

where μ is the cosine of the angle θ between the $\hat{z}$-axis and a vector from the surface area element $dx\, dy$ to the detector position and r is the distance from the surface area element to the detector.

$$r^2 = (x_D - x)^2 + (y_D - y)^2 + (z_D - 0)^2$$

$$\mu = \cos(\theta) = {}^{z_D}/_{r}$$

For the case of an emitter uniformly distributed through a thick slab, the directional distribution of the uncollided surface leakage current is $j(\mu) = 2\mu$. Using this approximation, the above integral reduces to

$$\phi \approx \frac{j_0}{2\pi} \int_{-B/2}^{+B/2} \int_{-A/2}^{A/2} \frac{z_D}{r^3}\, dx\, dy \quad .$$

Note that the solid angle Ω subtended by the slab from the point of view of the detector position is a similar integral

$$\Omega = \int_{-B/2}^{+B/2} \int_{-A/2}^{A/2} \frac{z_D}{r^3}\, dx\, dy \quad ,$$

so the flux can be expressed as

$$\phi \approx \frac{j_0\, \Omega}{2\pi} \, .$$

The LLNL USS computes the flux ϕ at a given detector position from a finite slab, using

	quantity	units
j_0	surface current per unit area, for an activity concentration of 1 Bq/kg	kg/cm^2
C	activity concentration	Bq/kg
S	surface area of slab	cm^2
Ω	solid angle of slab from the view of detector	ratio (0 to 2π)

to be

$$\phi = C\frac{j_0\, S\, \Omega}{2\pi}$$

where the solid angle of the slab as seen from the detector, Ω, is found by a Monte Carlo process of throwing rays from the detector position. By using the solid angle from the detector, the LLNL USS approach is basically assuming the surface leakage current directional distribution $j(\mu) = 2\mu = 2\cos(\theta)$, which may not be a good assumption for the cases for scattered photons or for thin slabs.

The LLNL USS approach for computing the flux at a detector position from a single finite slab was compared to 3D Monte Carlo estimates. For a simple slab of concrete with a ^{40}K concentration of 1 Bq/kg, a density of 2.3 g/cm^3, a length of 500 cm, a width of 250 cm and a thickness 11 cm, the fluxes for five series of detector positions were computed with MCNP. The total current per unit surface area for an infinite slab, j, was also computed (0.0011349 photons/cm^2/sec). The MCNP simulations included a layer of zero importance around the edges of the 11 cm thick slab so that only photons leaving the main face of the slab would be counted in the MCNP flux. The five series of detector positions (shown in **Figure 3**) compared included:

1. Along the normal direction from the center of the slab, from 1 to 100000 cm (red)
2. Along the normal direction, away from the center of the slab, 1 to 100000 cm (green)
3. Along the normal direction, far away from the center of the slab, 1 to 100000 cm (blue)
4. Along the width axis, 1000 cm distance, with angles from the normal of 0 to 85° (yellow)
5. Along the length axis, 1000 cm distance, with angles from the normal of 0 to 85° (purple)

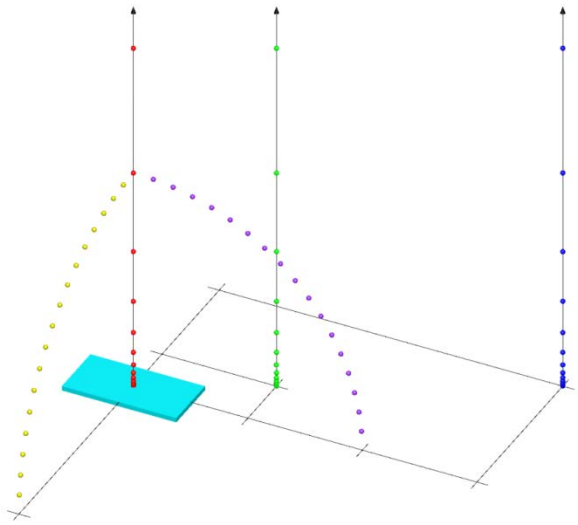

Figure 3. Series of detector positions

The five series of flux values from both the LLNL USS approach and MCNP are shown in **Figure 4**.

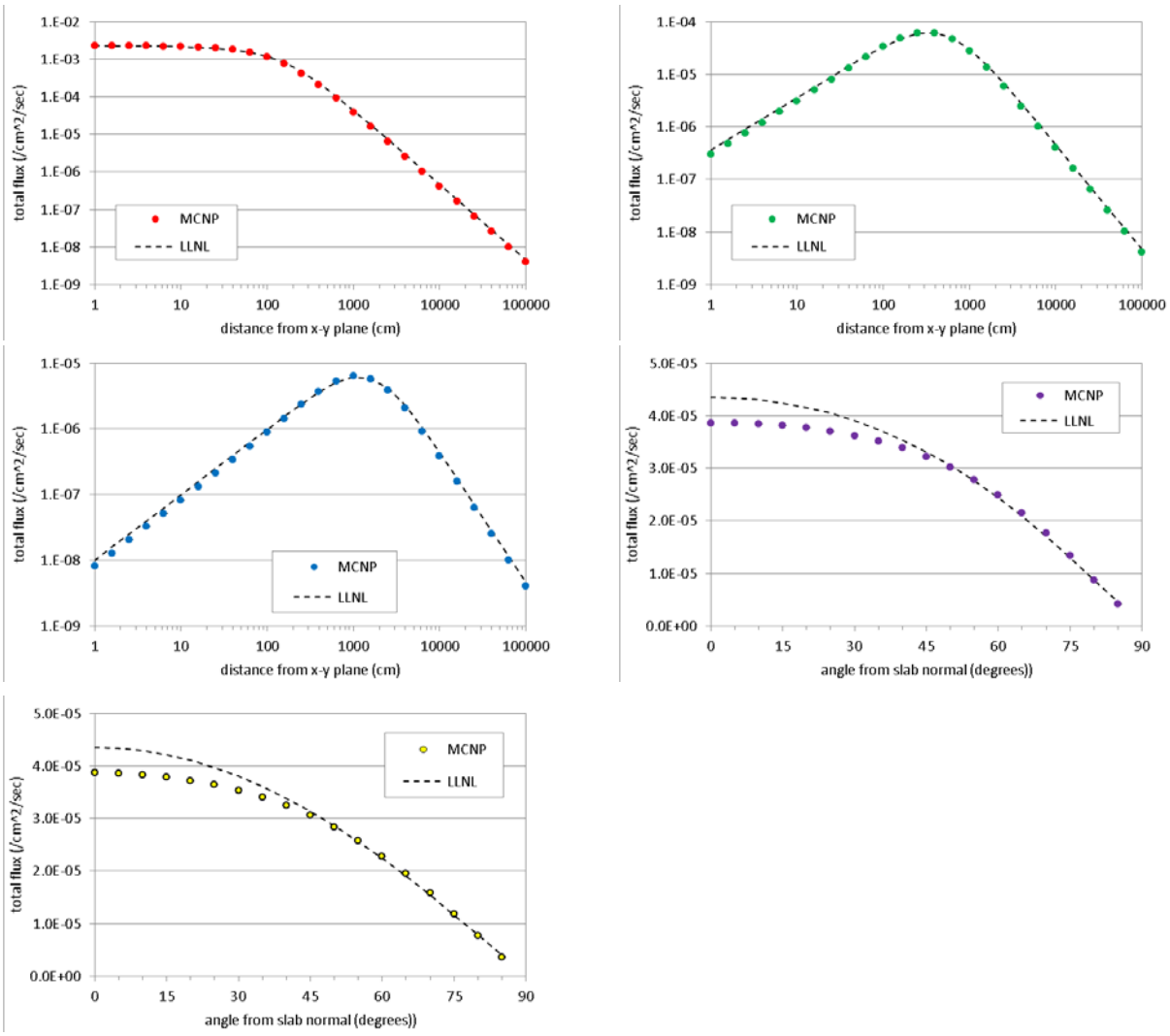

Figure 4. Total flux at the detector for the five series of positions corresponding to **Figure 3**.

Overall, the LLNL USS approach for finding the flux at the detector position from a single finite slab is fairly close to the 3D Monte Carlo simulations. The maximum error for the range of slab sizes and detector distances used in this study was an over-prediction by about 15%. A more complicated expression for the angular dependence of the surface leakage current was explored that gave results closer to the 3D Monte Carlo results. But this method was deemed too complicated for the small improvement.

Potential improvements in the speed of the LLNL USS include replacing the Monte Carlo ray-tracing algorithm for finding the solid angle of the slab with either a numerical integration or a simple analytic formula (Rajpoot, 2014) to save time. Although the analytical formula is suitable for surfaces right in front of the detector, its exact computation becomes extremely complex as solid angles of multiple surfaces intersect, rendering it time consuming as compared to the current ray tracing approach, for which it was verified that only 1000 rays are sufficient to estimate the solid angle within a reasonable accuracy and its complexity remains the same regardless of the scene geometry.

4 Simple Test of Multiple Slabs

The LLNL USS finds the total flux at the detector as the simple sum of the flux from each slab source in a given scene. While very fast, this approach cannot account for the scatter from other slabs in the scene, which would tend to increase the flux arriving at the detector. To demonstrate the impact of the fast approximation, a simple study was performed with SCALE/MAVRIC using three emitting slab sources.

The slab sources were:

- brick, 11 cm thick, ^{40}K source of 35 Bq/kg (red)
- concrete, 30 cm thick, ^{238}U/^{235}U source of 1 Bq/kg (green)
- granite, 15 cm thick, ^{232}Th source of 1 Bq/kg (blue)

Note that the strength of the ^{40}K source was scaled up so that its flux at the detector would be comparable to the other fluxes.

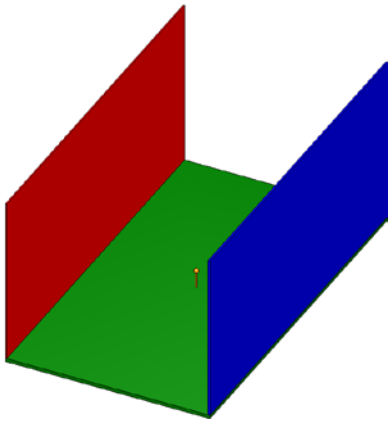

The objective was to compute the flux at a single position (yellow sphere) that is 700 cm from the brick surface, 150 cm above the concrete and 1000 cm from the granite surface. Two approaches were used: each slab source independently simulated and added together and a full simulation including scatter.

By ignoring scatter from slabs close to the detector, the LLNL USS approach under-predicts the low-energy flux arriving at the detector. **Figure 5** shows the ratio of two simulations, with and without the LLNL simplifying assumption. (Note that artifacts at higher energies are the result of dividing two data sets each with high uncertainties.) At lower energies, the under-prediction by the single-slab-at-a-time approach is quite pronounced.

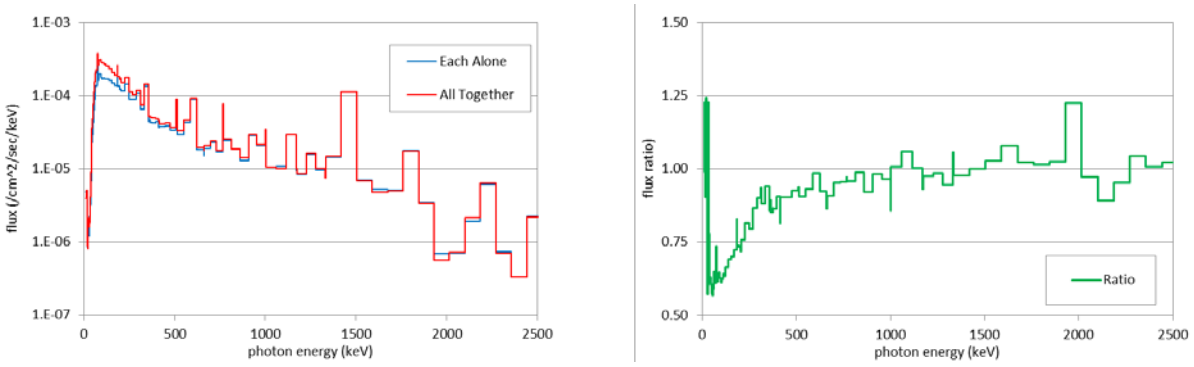

Figure 5. Energy dependent flux at the detector (left) for two methods and their ratios (right).

5 Detector Response

The 3D Monte Carlo tools can compute the energy deposited in a detector region, but that requires having the detector present in the model. Typically, the Gaussian spreading of the measured spectrum seen by real detectors is not part of the MC particle transport process and is applied outside of the MC code. When performing calculations of detector count rates at many places at once, the detector would have to be present at each location, which could shield or direct scattered photons to the other detector locations.

For these reasons, when using general MC codes to compute detector response, a two-step process is used.

For the first step, a response function for converting a mono-energetic flux into an energy-deposited spectrum is constructed for the range of possible incident photon energies (Gardner & Sood, 2004). This can be done assuming the photons only enter one face of the detector, several faces, or from any direction. For detectors that have aspect ratios far from one, there can be large differences in the response for different faces. For situations where the detector is expected to be exposed from any direction, the detector response can be constructed using a source uniformly around the detector.

For the Urban Search project, the omni-directional approach was used. MCNP was used to simulate a NaI detector inside a spherical source, with mono-energetic photons directed inward, shown in **Figure 6**. The source strength was set to be equal to the square of the radius of the sphere, so that the flux inside the sphere without the detector present would be 1. Two thousand simulations were done for source energies between 2 keV and 4000 keV. The energy deposited spectrum computed by MCNP (F8 tally) for three different source photon energies are shown in **Figure 7**.

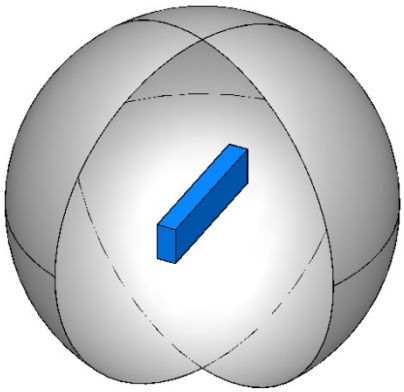

Figure 6. NaI detector exposed to mono-enegetic photons started on the surface of a sphere directed inward.

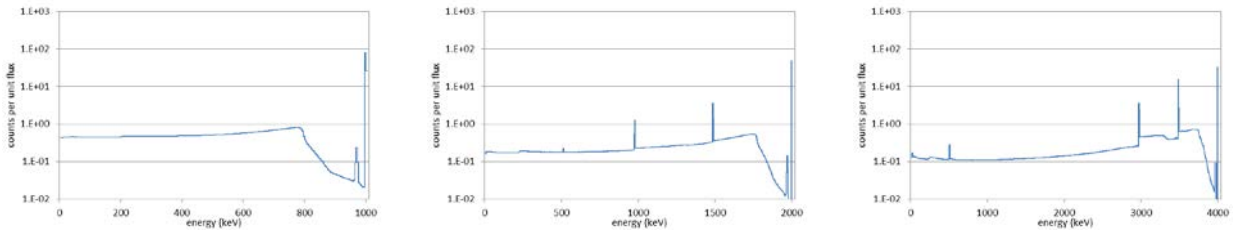

Figure 7. Energy deposited in the NaI computed for 1000 keV, 2000 keV and 4000 keV from a unit flux of omni-directional photons.

In the second step, the 3D simulation computes the energy-dependent photon flux in every part of the model where a detector could be placed, but does not actually contain the detector model anywhere. The fluxes from the simulation are then combined with the above pre-computed response function to determine the energy-deposited spectrum in the detector, had it been explicitly modeled.

The two-step approach described above saves quite a bit of computational time, but has the disadvantage of not taking into account the direction that the photons actually came from. For detectors with large aspect ratios, the difference in the true response among different detector orientations can be large. For low-energy photons, the response is roughly proportional to the surface area of the detector facing the source. For higher-energy photons, the response is roughly proportional to the surface area of the detector facing the source multiplied by the probability of interacting within the chord length through the detector. For a 2×4×16 inch NaI, very different responses will result from different detector orientations.

The response function above can also be used to look at total counts as well. For a given mono-energetic flux, the number of counts recorded by the detector is the sum of energy-deposited spectrum for that incident energy. **Figure 8** shows the number of counts for a flux of mono-energetic photons striking the NaI detector from any direction. Note that the values are large (170-300 counts per unit flux) over most of the energy range. This is due to the large volume of the detector (2097.54 cm^3).

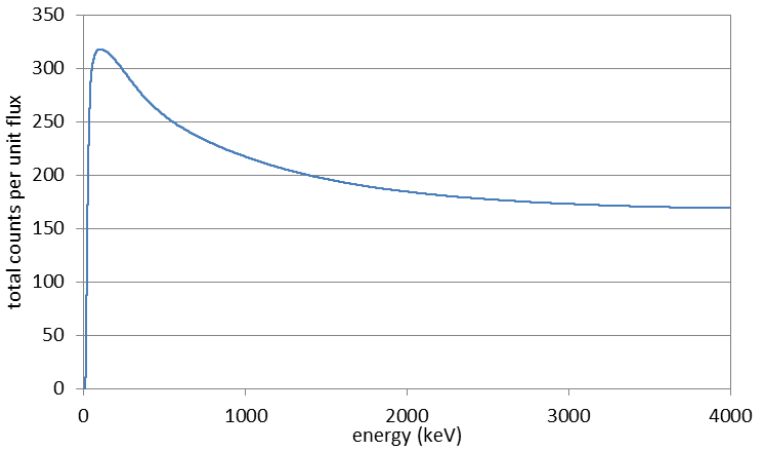

Figure 8. Factor for converting mono-energetic flux to total counts.

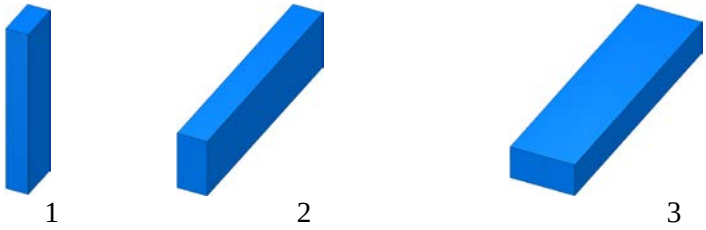

Figure 9. Three orientations of the detector, with photon incident from below.

Detector responses for photons striking the detector from below in three orientations will give three different responses. For example, the detector responses of 1 MeV photons for the three orientations shown in **Figure 9** are shown in **Figure 10**.

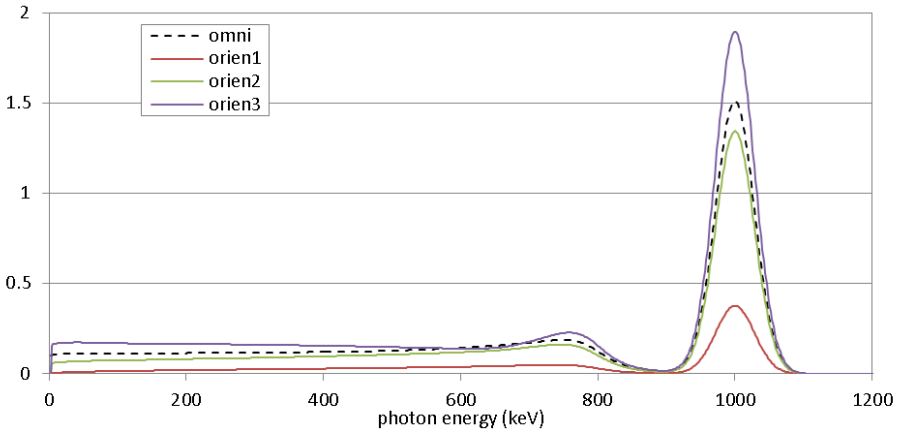

Figure 10. Detector response using different response functions.

5.1 Detector Response Test from a Single Slab

The test problem is a single granite slab (2.69 g/cm^3), 11 cm thick, with 1 Bq/kg of ^{40}K, ^{232}Th, or ^{238}U/^{235}U) at a distance of either 1 or 10 m from the center of the detector (see **Figure 11**).

This test will compare the spectra from

1. MCNP pulse-height tally (energy deposited) with the detector in one of three orientations
2. MCNP flux tally with the detector outline in one of three orientations, combined with omni-directional detector response function

The counts as a function of energy will be shown with and without the energy resolution function applied.

The detector is a 2" × 4" × 16" NaI (5.08 × 10.16 × 40.64 cm), surrounded with 1 mm of aluminum.

The three orientations considered are where the photons emitted perpendicularly from the slab surface strike:

one of the 2" × 4" faces,
one of the 2" × 16" faces, or
one of the 4" × 16" faces

of the detector. The results are shown in **Figure 12** below.

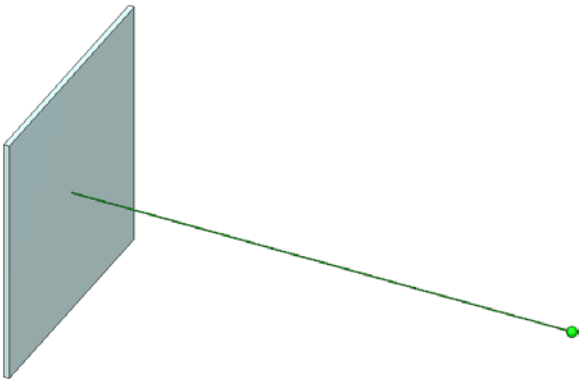

Figure 11. Geometry: 5m × 5m × 11cm, detector 10 m away.

Two observations can be made from this test:

1. The method of computing flux and convolving with the detector response function (red) produces very similar results independent of detector orientation. This is because the flux varies slowly over the detector region (which small compared to dimensions of the test problem).
2. The calculated energy-deposited in the 2"×4"×16" NaI detector, when it is directly modeled, does change with detector orientation. The computed energy deposited spectrum for a detector at 10 m shows this effect quite dramatically – at this larger distance, a greater fraction of the photons entering the detector come through the face that is parallel to the slab.

For detectors with nearly uniform dimensions (3"×3", 6"×6"), generating and using a response function is fairly straightforward. Flux can be computed and then convolved with a single detector response function to compute the count rate had the detector been in the simulation.

For detectors with a high aspect ratio, a large difference in response can be seen among photons striking different faces. Since the typical flux tally does not know how much of the flux came from different directions, a single detector response function is not going to work. Additions to the Monte Carlo code such as storing which source the photon started from or which region its last collision was in could be made. Storing flux moments and combining them with different detector responses functions for each face could be another way to approximate the response from a high aspect ratio detector.

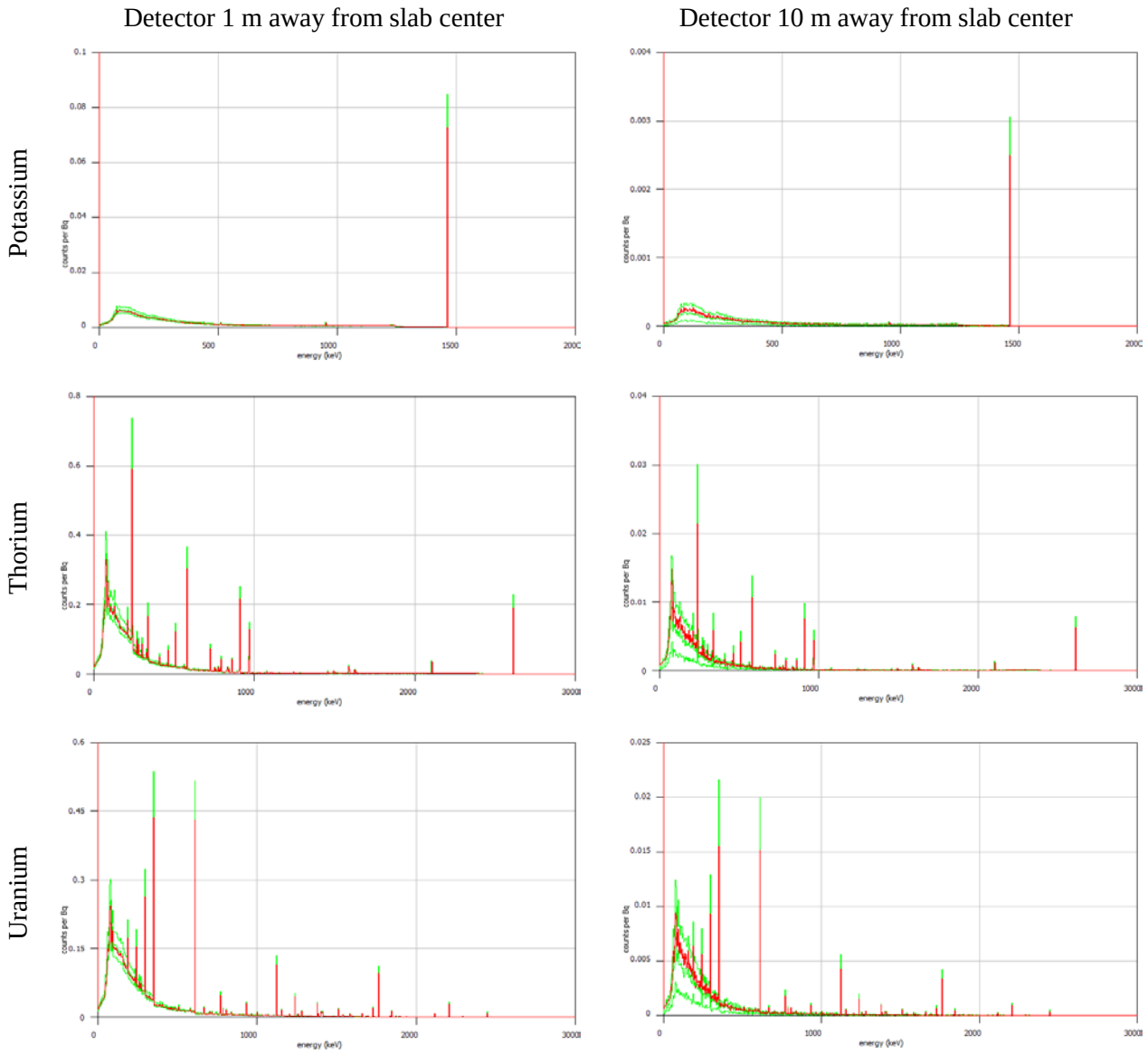

Figure 12. Computed energy deposited spectra for (green) MCNP pulse-height tally with detector in a given orientation and (red) MCNP flux tally combined with omni-directional detector response function.
Note: Each plot has 3 green lines and 3 red lines. The red lines are very similar.

5.2 Detector Energy Resolution

The energy deposited pulse-height tallies above represent the spectrum that a perfect detector would record. For a given amount of energy deposited in the active region of a real detector, the final signal produced by the counting system has some uncertainty. This can be represented by a Gaussian distribution about the true energy deposited.

A routine was written to apply a Gaussian spread function to the MCNP energy deposited (pulse-height) spectrum. This routine uses the GADRAS equations and parameters for the full width at the half maximum (FWHM) of the distribution as a function of incident energy (Mitchell, 2014).

	E_{crit} (keV)	w (keV)
Non-HPGe	661	$0.01\ P_7 E_{\text{crit}}$
HPGe	1332	P_7

$$\text{FWHM} = \begin{cases} w\left(\dfrac{E}{E_{\text{crit}}}\right)^{P_8} & E > E_{\text{crit}} \\ \sqrt{\left[P_6\left(\dfrac{E_{\text{crit}}-E}{E_{\text{crit}}}\right)\right]^2 + \left[w\left(\dfrac{E}{E_{\text{crit}}}\right)^{P_8}\right]^2} & E \le E_{\text{crit}} \text{ and } P_6 \ge 0 \\ w\left(\dfrac{\max(E, E_{\text{low}})}{E_{\text{crit}}}\right)^{P_8^{\left[\frac{1}{\ln(1-P_6)}\right]}} & E \le E_{\text{crit}} \text{ and } P_6 > 0 \end{cases}$$

where the parameters P_6, P_7, and P_8 are supplied by the user and E_{low} =20 keV.

Figure 12 displays examples of the energy deposited for a given mono-energetic flux striking a 2x4x16 inch NaI detector with 1 mm Al. Also shown is that same information with the detector response applied (7.5% FWHM at 661 keV and an energy power of 0.7).

5.3 New USS Detector Response

The new USS detector response uses slabs as sources as opposed to spheres, as GADRAS slab modeling has been fixed in newer versions. A 1 kg piece of material with activity of 1 Bq is modeled for slabs with different thicknesses, materials and isotopes as previously described. The detector response is then calculated for a desired detector positioned 100 cm from the slab. For each slab, its solid angle is computed according to the following formula for the solid angle of a pyramid:

$$\Omega = 4\ arctan\left(\frac{l^2}{2d\sqrt{4d^2+2l^2}}\right)$$

where d is the distance from the slab to the detector and l is such that $\frac{1}{\rho l^2}$ is the desired thickness of the slab, where ρ is the material density of the slab. Thus, for a surface with estimated solid angle by ray tracing $\widetilde{\Omega}$, if Ω is its corresponding source slab (i.e., same usage, material, thickness and isotope) which produced x counts, then the detector response will have y counts, where $y = \frac{\widetilde{\Omega}}{\Omega}x$.

500 keV

1000 keV

1500 keV

2000 keV

4000 keV

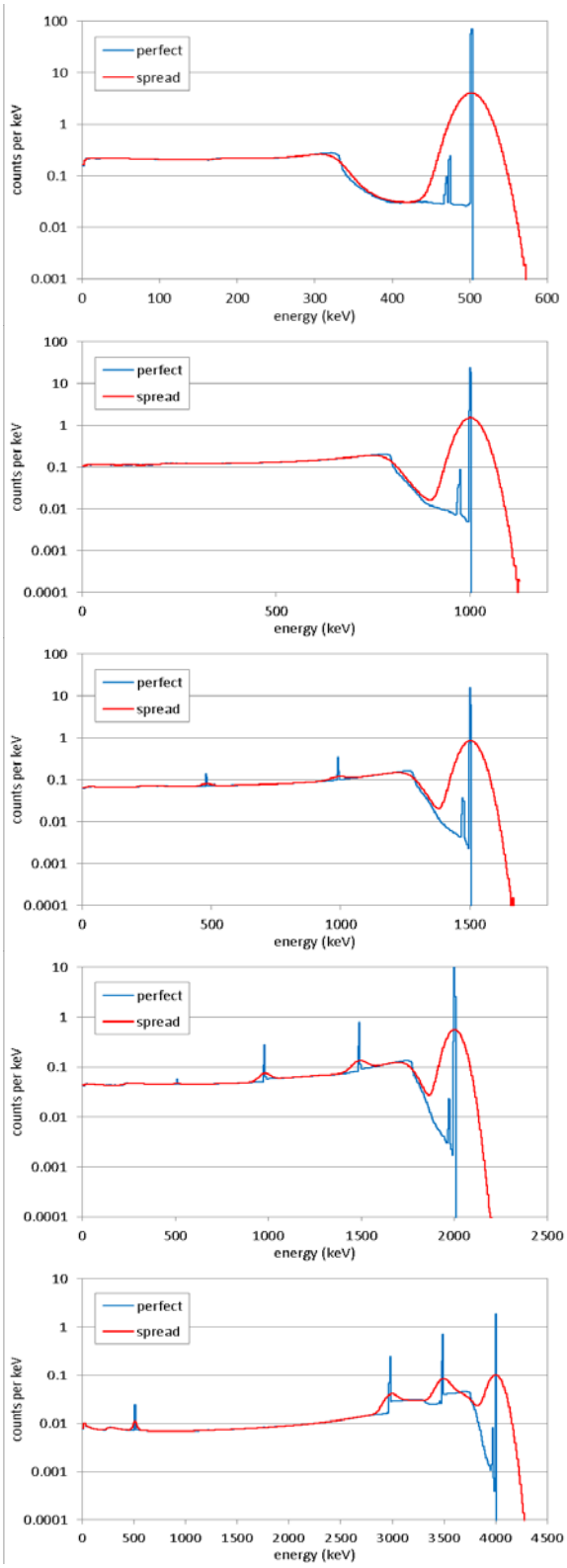

Figure 13. Computed energy desposited spectra with and without detector resolution.

6 Full Scene Comparisons

To create an optimized search route, the background at every possible detector location needs to be known. The LLNL USS is quite fast but uses some approximations. The impact of the approximations can be seen by comparing the calculated values of the detector count rates along the streets to calculations performed using a rigorous 3D Monte Carlo code. For a section of an urban environment that could be several blocks in size, Monte Carlo calculation times could be very long.

Monte Carlo Simulations

Monte Carlo particle transport calculations for deep penetration problems can require very long run times in order to achieve an acceptable level of statistical uncertainty in the final answers. Discrete ordinates codes can be faster, but have limitations relative to detailed geometry modeling and large memory requirements. Monte Carlo calculations can be modified (biased) to produce results with the same variance in less time if an approximate answer or some other additional information is already known about the problem. Over time, there have been many Monte Carlo variance reduction methods developed and used. One of the most successful methods has been weight windows, which controls the weights of particles in a portion of phase space by splitting high-weight particles and rouletting low-weight particles. The difficulty with weight windows for analysts is mostly in assigning weight window values as a function of both space and energy. Another problem commonly encountered with weight windows is determining the source biasing properly so that source particles are not immediately split or rouletted just after birth, which could reduce the overall effectiveness of the variance reduction.

It has been recognized for a long time that the adjoint solution to a source/detector problem represents the importance of particles to contributing to that detector and that weight windows in a Monte Carlo code should be inversely proportional to the importance of a particle. Wagner and Haghighat [Wagner, 1998; Haghighat, 2003] developed the Consistent Adjoint Driven Importance Sampling (CADIS) method to develop weight window target values and consistent source biasing parameters which would optimize the Monte Carlo calculation for the calculation of an integrated response at a single detector location. The source used in the adjoint calculation is detector response function at the location of the detector. Methods that use a deterministic solution to develop the biasing parameters for the Monte Carlo calculation are now referred to as 'hybrid methods'. For a variety of deep penetration source/detector problems, the CADIS method can greatly reduce the Monte Carlo statistical uncertainty or required calculation time.

The CADIS method has been extended to optimize large mesh tallies by creating an importance map that converges the high-flux areas and the low-flux areas of the mesh tally at nearly the same rate, giving more uniform relative uncertainties across the mesh tally. The forward-weighted CADIS method (FW-CADIS) [Wagner, 2014] uses the deterministic estimate of forward flux in creating the adjoint source. The adjoint source still has the energy distribution of the detector response function but has a spatial extent covering the mesh tally to be optimized, with the amount of adjoint source inversely proportional to the forward flux estimate. Like CADIS, both weight window target values and consistent source biasing parameters are produced. Both the CADIS and FW-CADIS methods have been implemented into the SCALE/MAVRIC package [Peplow, 2011] which uses the Denovo discrete ordinates code [Evans, 2010].

LLNL Model Scene Generator

The scene generator models blocks, streets and buildings. Blocks and streets are modeled as ground.
For each scene, the number of blocks in the x-direction as well as in the y-direction is an input parameter. The block dimensions are generated from a truncated Poisson distribution for both axes. For the x-axis, the parameters for the minimum/mean/maximum are 40/70/100 m. For the y-axis, the same parameters are 30/50/70 m. Street widths are generated according to a truncated Poisson distribution with

minimum/mean/maximum parameters of 10/20/30 m. After building the blocks and streets, the LLNL USS divides each block into lots. For each block, it is determined whether its depth in the y-direction is one or two, i.e., if it will have one or two lots in the y-direction. The probability that it will have only one lot is set to 0.2. If there are two lots on the y-direction, the ratio between them will be drawn from a uniform distribution with parameters minimum 0.4 and maximum 0.65. The lot size on the x-direction is drawn from a uniform distribution with a minimum of 10 m and maximum of 40 m. Finally, a lot will have a building or will be empty. The probability that a lot will be empty was set differently for each test. If a lot contains a building, the ratio of the area of the base of the building to the lot is drawn from a uniform distribution with a minimum of 0.9 and a maximum of 0.91. Building heights are generated from truncated Poisson distribution with parameters varying for each test set.

For all scenes, the probability of a wall being made of granite, brick and concrete is 0.5, 0.25 and 0.25 respectively. Ground is made of concrete. Concentrations of the radioactive isotopes in the wall and ground materials are generated from truncated Gamma distributions. The parameters are shown in **Tables 2-4** below for each isotope. The parameters are the minimum (min), maximum (max), mean, standard deviation (std) and the fraction of the pdf to put in tail (last column).

Table 2. Distribution of concentration values for Th232

usage	material	min	max	mean	std	fraction tail
wall	granite	0	158	35	35	0.01
wall	brick	1	220	44	44	0.01
wall	concrete	7	240	21	15	0.01
ground	concrete	7	120	21	15	0.01

Table 3. Distribution of concentration values for U238

usage	material	min	max	mean	std	fraction tail
wall	granite	116	1176	33	35	0.01
wall	brick	7	177	111	35	0.01
wall	concrete	15	196	46	30	0.01
ground	concrete	15	98	46	30	0.01

Table 4. Distribution of concentration values for K40

usage	material	min	max	mean	std	fraction tail
wall	granite	800	3054	1384	170	0.03
wall	brick	5	1600	666	170	0.03
wall	concrete	24	850	300	170	0.03
ground	concrete	24	425	300	170	0.03

For this comparison, a 6×6 inch cylindrical detector is used to remove the difficulty of handling the orientation of the 2×4×16 inch (5.08×10.16×40.64 cm) sodium iodide detector. In addition, the USS used ORIGEN and MCNP to generate the count rates for 1 Bq of each radioisotope from every combination of material and thickness at 100 cm. The NORM concentrations in the intersections used the values from the north-south streets.

The models used by both the LLNL USS and the SCALE/MAVRIC simulations used the material data shown in **Table 5**, taken from a PNNL report [McConn, 2011].

Table 5. Material composition data used in the scenes

		concrete	granite	brick
Weight Percent	H	2.2100		
	C	0.2484		
	O	57.493	48.417	52.5
	Na	1.5208	2.7328	
	Mg	0.1266	0.4274	
	Al	1.9953	7.6188	0.5
	Si	30.4627	33.6169	44.9
	K	1.0045	3.4144	
	Ca	4.2951	1.2985	1.4
	Ti		0.1795	
	Mn		0.0387	
	Fe	0.6435	2.1555	0.7
	Pb		0.1004	
Density g/cm^3		2.3	2.69	1.8

A series of 3x3-block scenes were generated using different densities and heights of buildings. For each scene, building heights were generated according to a truncated Poisson distribution, with minimum/mean/maximum of 10/15/20 m. For this set of scenes, the probability that a lot would be empty was set to:

- *Scene 13*: only one building;
- *Scene 14*: 0.50;
- *Scene 15*: 0.01.

Additional 3x3-block scenes were generated using taller building heights. For the scenes with the taller building heights, truncated Poisson distributions used minimum/mean/maximum values of 20/50/80 m. For this set of scenes, the probability that a lot would be empty was set to:

- *Scene 21*: 0.90;
- *Scene 22*: 0.50;
- *Scene 23*: 0.01.

The purpose of these test sets is to show impact the geometry of scene has on the difference between the 1D and 3D approaches. For each scene, three plots are shown: a 3D plot of scene, 2D plot showing count rate (counts per second) for MAVRIC and also a 2D plot showing the relative difference between MAVRIC and USS as Diff $= \frac{B_{MAVRIC} - B_{USS}}{B_{MAVRIC}}$. For all the scenes, the LLNL USS took less than 1 minute of cpu time to calculate the background at all detector locations.

Scene 13

The first test was a 3×3 block area with a single building. The continuous-energy Monte Carlo solution using SCALE/MAVRIC used 15 hours of cpu time and resulted in count rates with < 2% relative uncertainty.

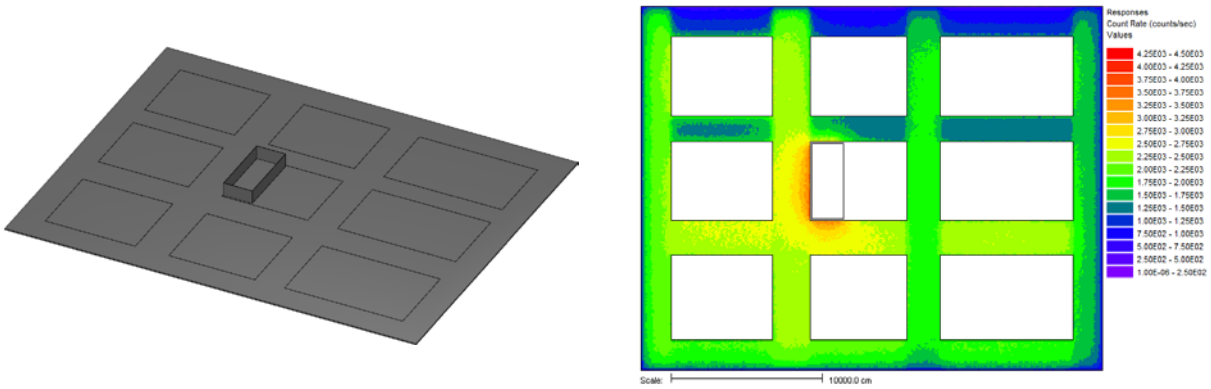

Figure 14. *Scene 13* geometry (left) and MAVRIC count rates in counts per second (right).

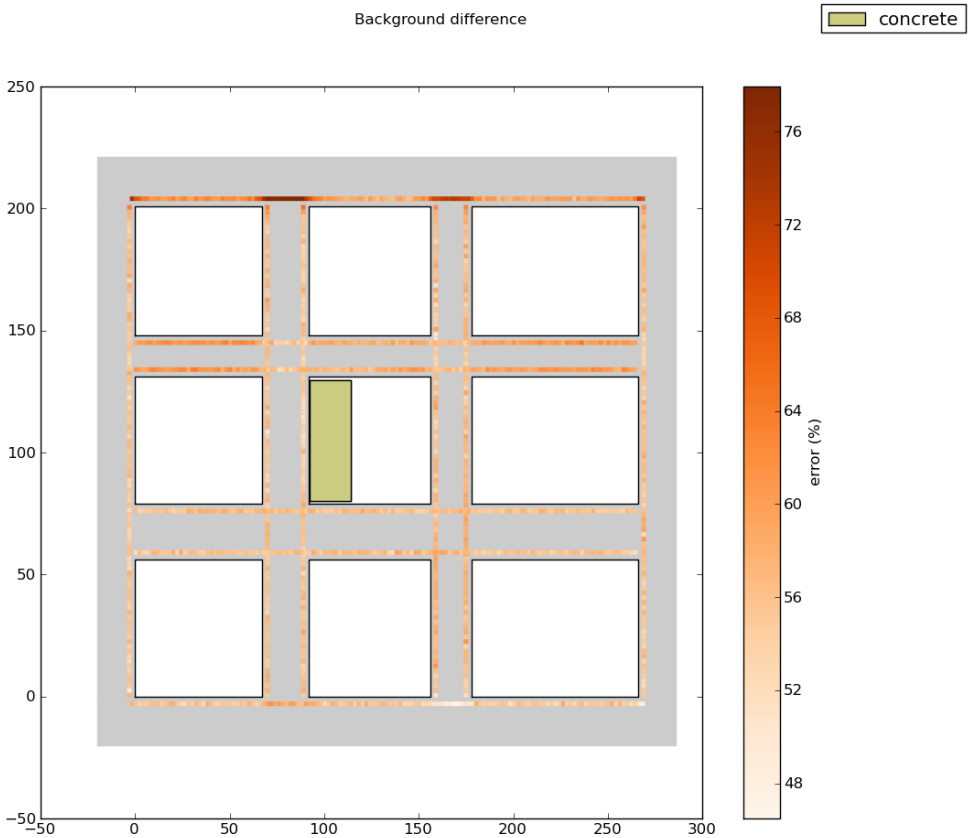

Figure 2. Relative difference in background count rate between USS and MAVRIC for *scene 13.*

Scene 14

The second test was a 3×3 block area with several buildings. Continuous-energy Monte Carlo solution using SCALE/MAVRIC used 15 hours of cpu time and resulted in count rates with < 3% relative uncertainty.

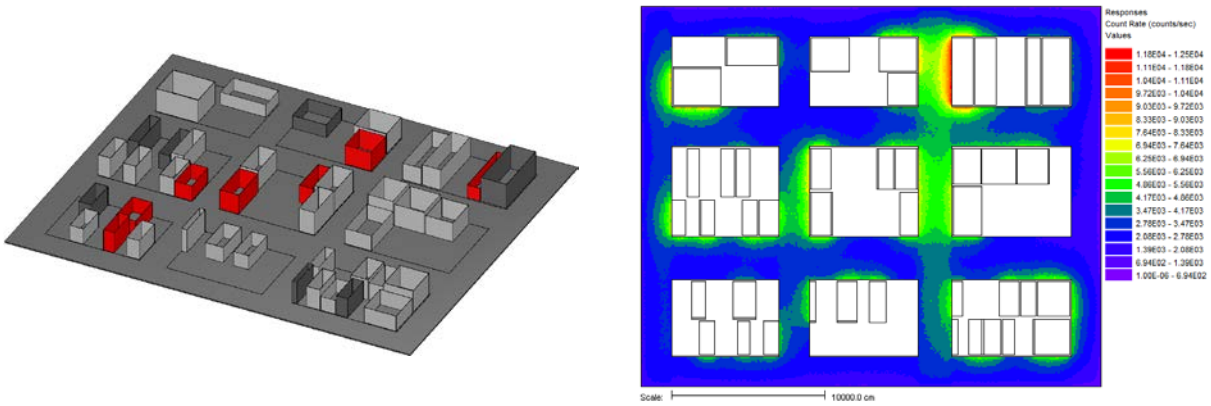

Figure 16. *Scene 14* geometry (left) and MAVRIC count rates in counts per second (right).

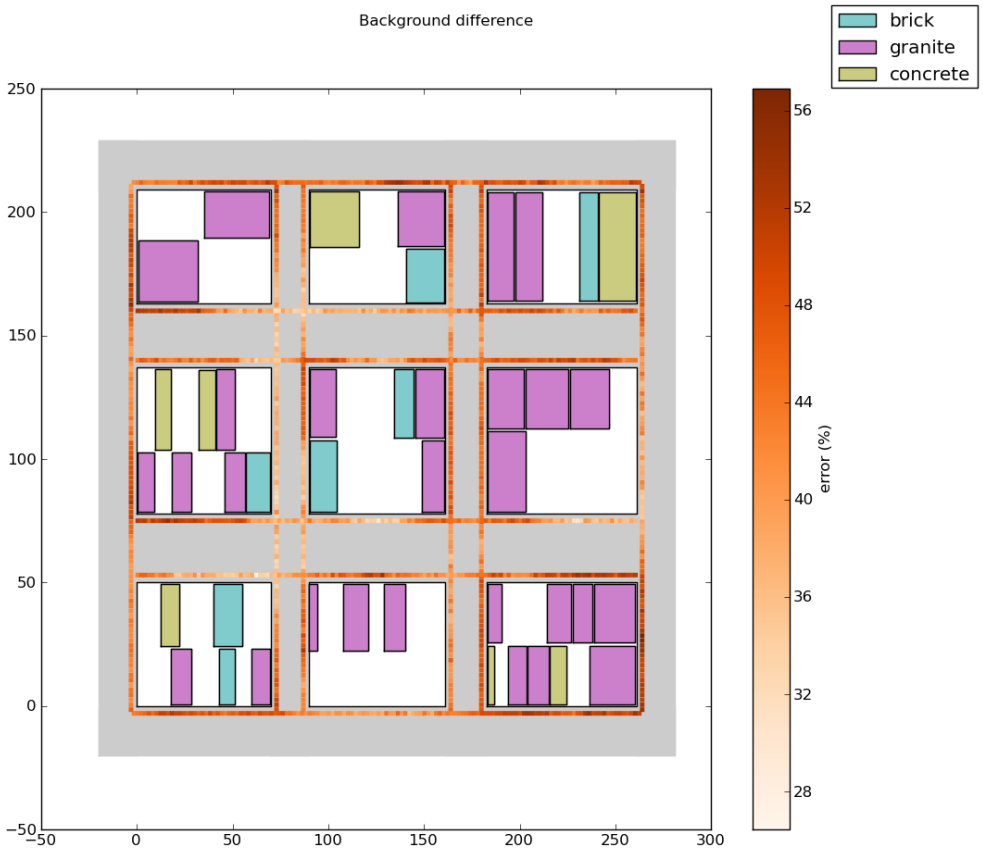

Figure 3. Relative difference in background count rate between USS and MAVRIC for *scene 14*.

Scene 15

The third test was a 3×3 block area filled with buildings. Continuous-energy Monte Carlo solution using SCALE/MAVRIC used 15 hours of cpu time and resulted in count rates with < 3% relative uncertainty.

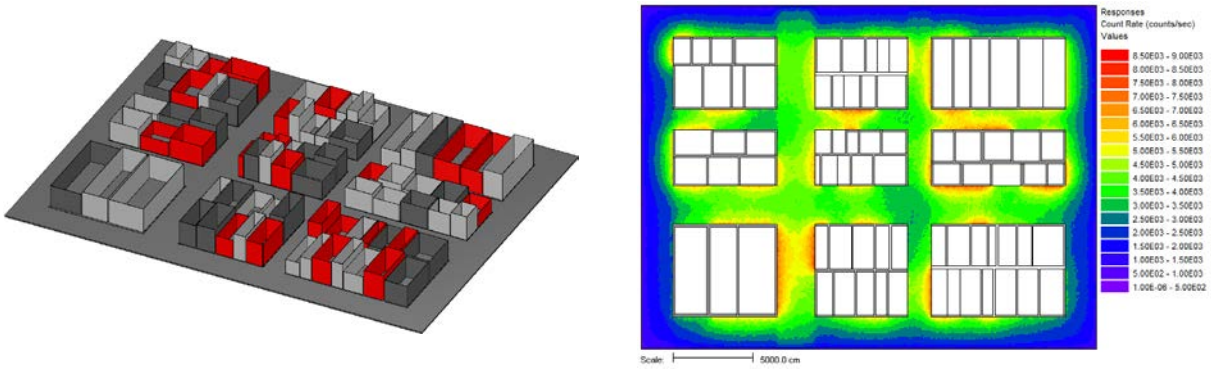

Figure 4. *Scene 15* geometry (left) and MAVRIC count rates in counts per second (right).

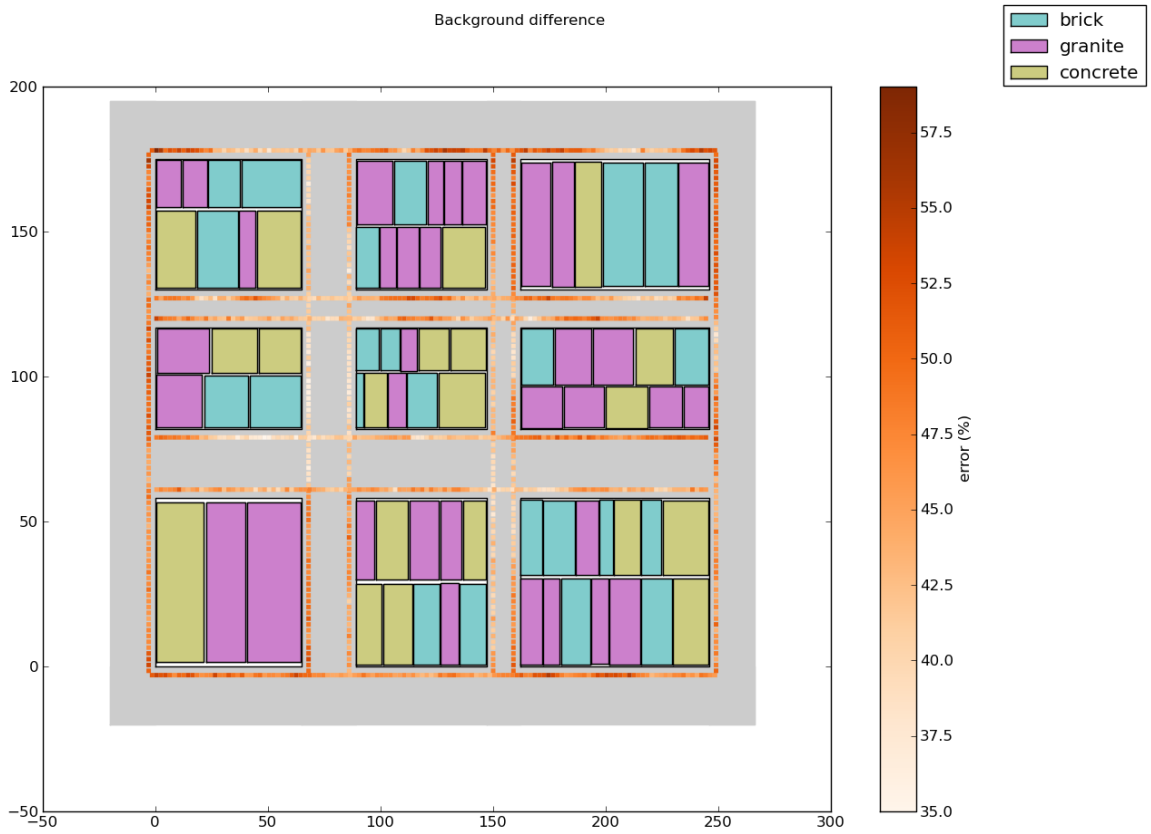

Figure 5. Relative difference in background count rate between USS and MAVRIC for *scene 15*.

Scene 21

Continuous-energy Monte Carlo solution using SCALE/MAVRIC used 15 hours of cpu time and resulted in count rates with < 2.5% relative uncertainty, typically 1.5%.

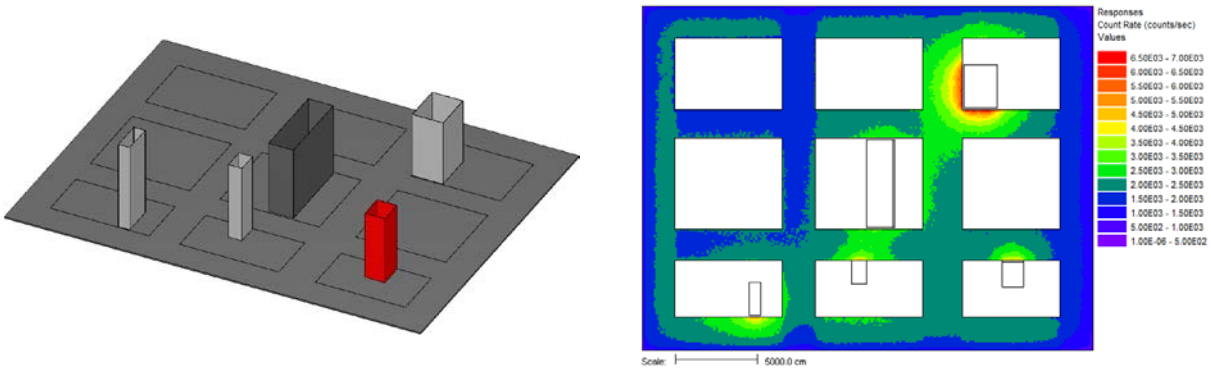

Figure 20. *Scene 21* geometry (left) and MAVRIC count rates in counts per second (right).

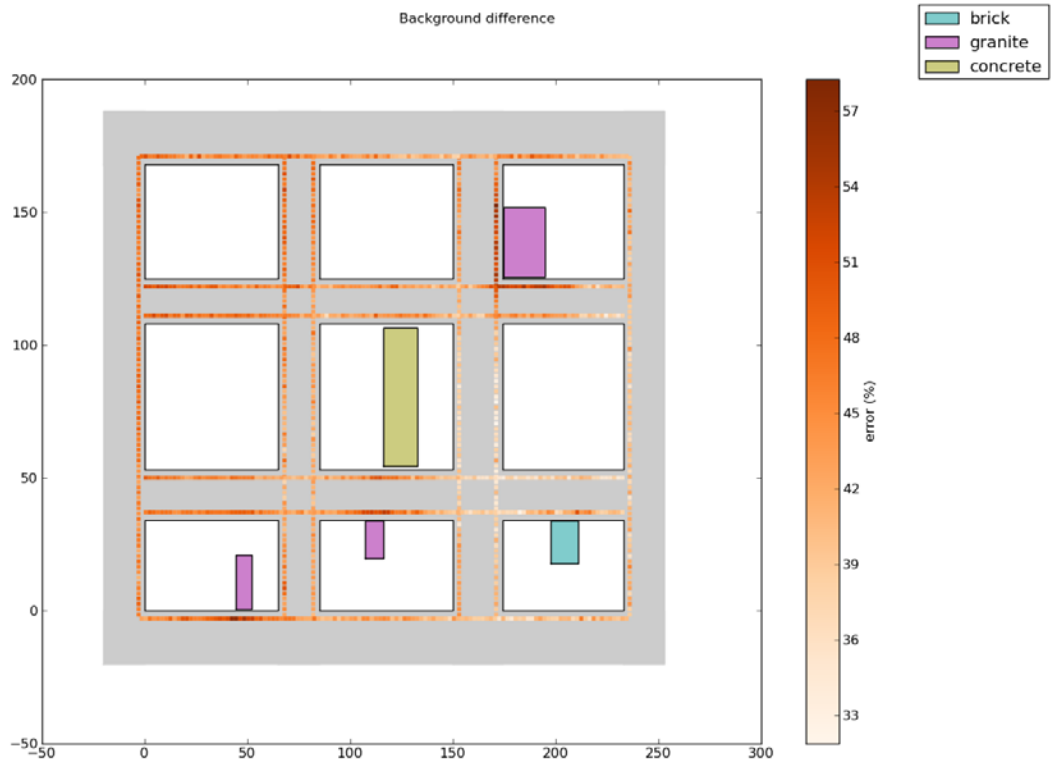

Figure 6. Relative difference in background count rate between USS and MAVRIC for *scene 21*.

Scene 22

Continuous-energy Monte Carlo solution using SCALE/MAVRIC used 15 hours of cpu time and resulted in count rates with < 3% relative uncertainty, typically 1.6%.

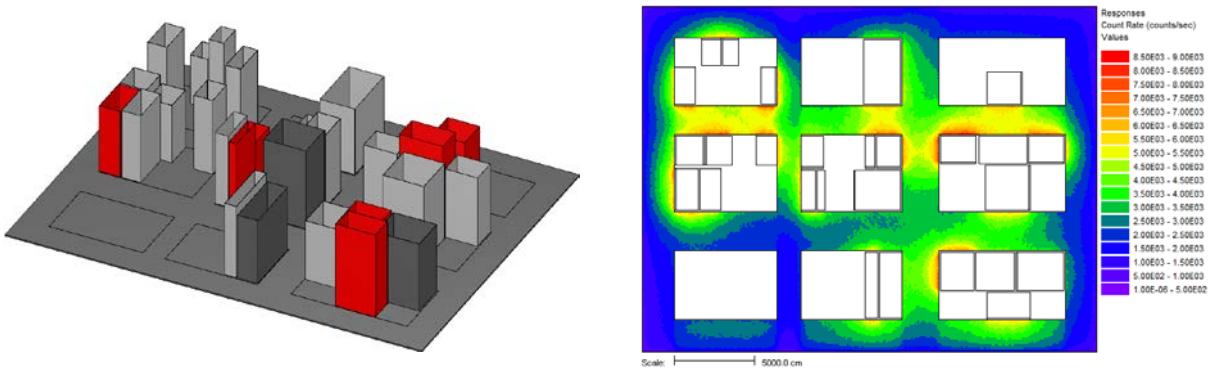

Figure 7. *Scene 22* geometry (left) and MAVRIC count rates in counts per second (right).

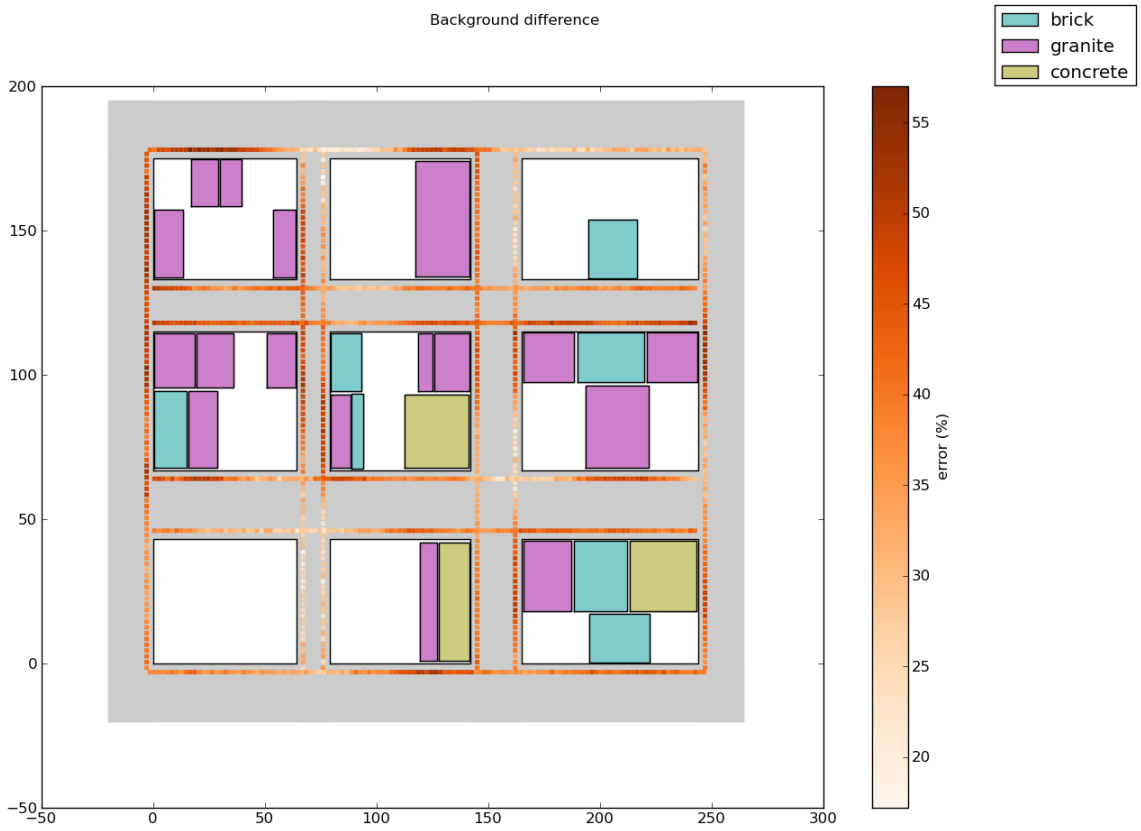

Figure 8. Relative difference in background count rate between USS and MAVRIC for *scene 22*.

Scene 23

Continuous-energy Monte Carlo solution using SCALE/MAVRIC used 15 hours of cpu time and resulted in count rates with < 10% relative uncertainty, typically 2%.

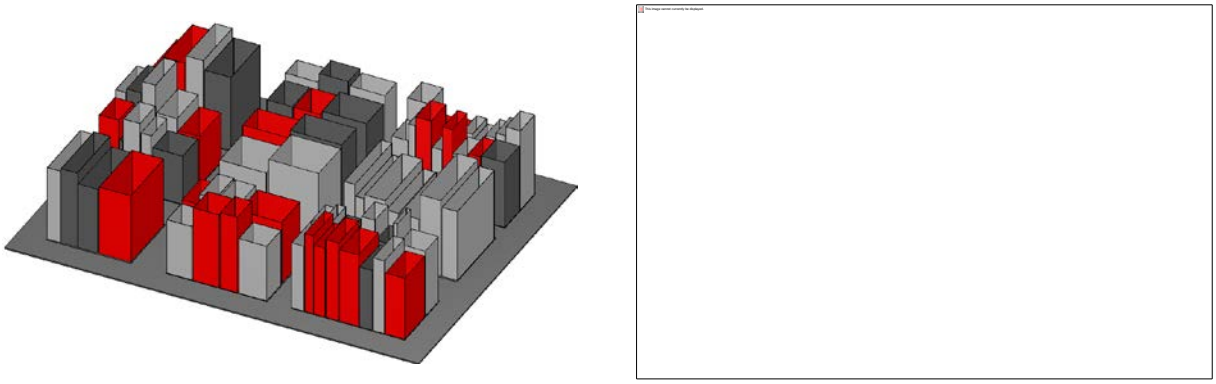

Figure 9. *Scene 23* geometry (left) and MAVRIC count rates in counts per second (right).

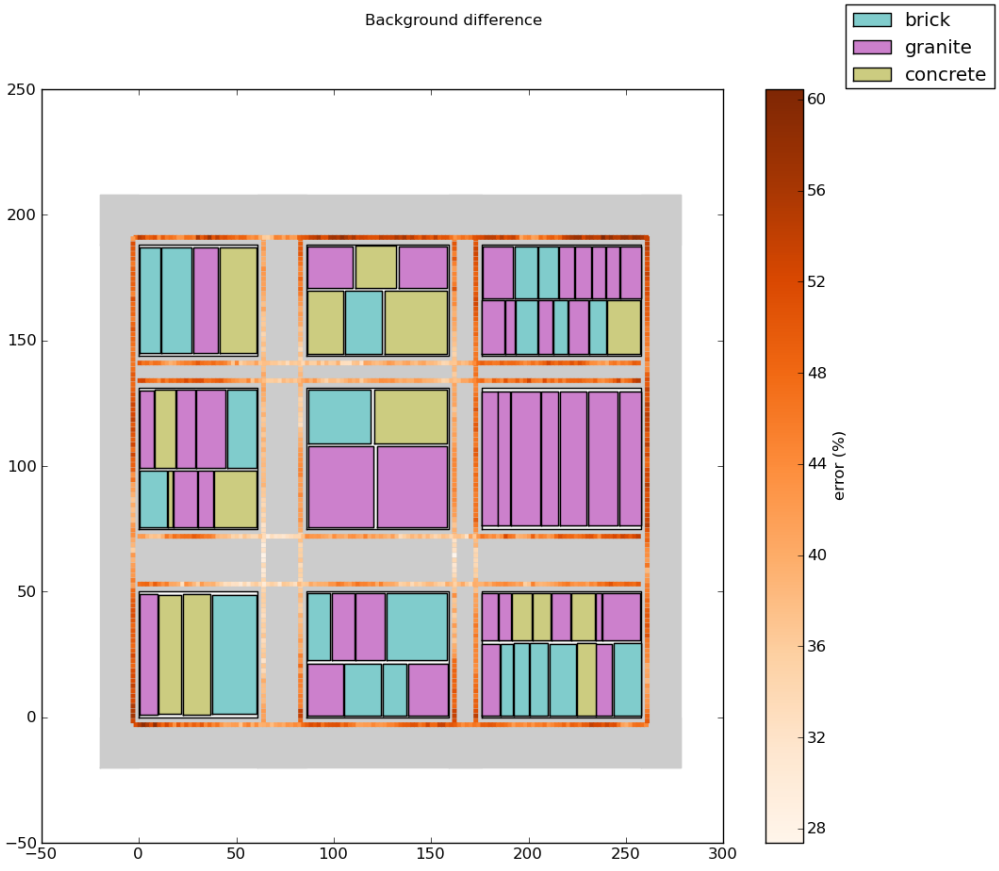

Figure 10. Relative difference in background count rate between USS and MAVRIC for *scene 23*.

7 Summary

For all the scenes, the relative difference in background count rate (Diff $= \frac{B_{MAVRIC} - B_{USS}}{B_{MAVRIC}}$) ranges from just under 30 to 60%, except for *Scene 13*, which had a few outliers with a maximum relative difference of around 78%. There was no significant change in the results (3-5%) both with respect to the number of buildings and buildings heights.

Comparisons of the count rates computed by the USS and MAVRIC are also shown in **Figure 26**. These show that, except for a few points in Scene 13, that the USS- and MAVRIC-computed count rates correlate quite well, but have a factor of two difference in magnitude. For Scene 13, the points at the lower portion of the plot, where the USS computes 500-600 counts/sec but MAVRIC computes 1600-2600 counts/sec, correspond to two roadway intersections along the northern-most east-west roadway.

The factor of two difference between the USS and MAVRIC is not explained by the smaller differences seen in the various steps going into the simulations. Work will continue to determine the cause of this mismatch between the two codes so that the real differences between the fast 1-D USS and rigorous 3-D MAVRIC can be demonstrated. In addition, we will look into the cause of the outliers in Scene 13.

Because of the high variance in the relative difference for different detector locations for all experiments done so far, more experiments with different scenes varying the probability of types of materials are necessary for a more complete estimate of the difference between MAVRIC and USS. *So far, most of the experiments show that the difference is highly dependent on the concentration of the isotopes, more so than on the geometry of the scene itself, as changes in building height or number of buildings did not change the overall results.* Thus, in addition to experiments varying material types, more analysis is needed in order to accurately characterize how the concentration values affect the difference between the approaches.

Scene 13

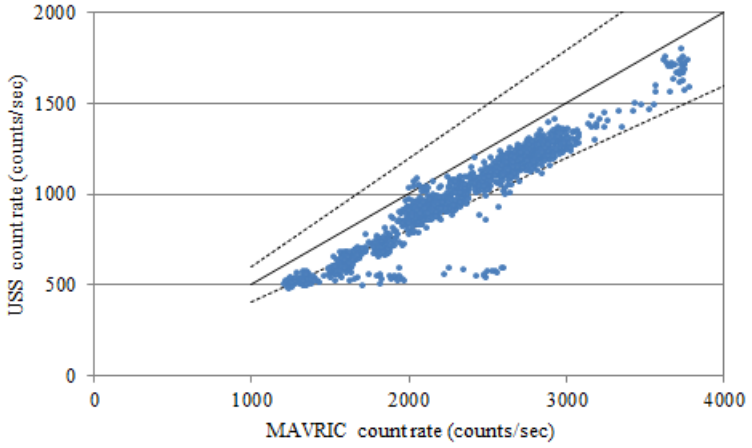

Scene 14

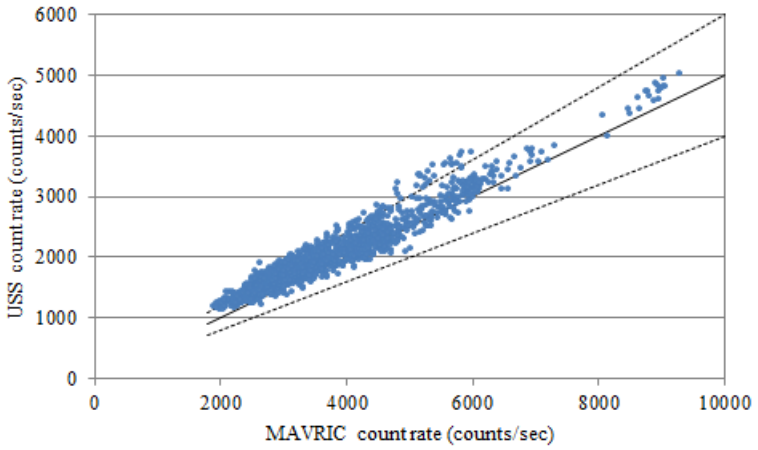

Scene 15

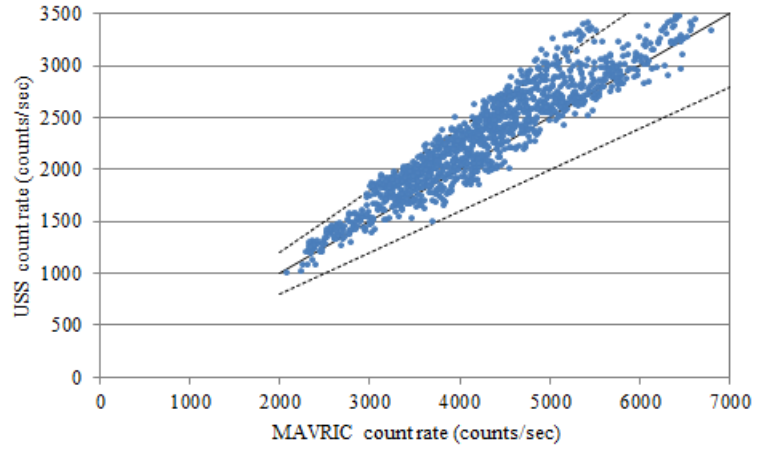

Figure 26. Correlation between USS- and MAVRIC-computed values of background count rates (counts/sec). The solid black line is a slope of 0.5 and the dotted black lines are slopes of 0.4 and 0.6.

References

Evans, Thomas. M., Alissa S. Stafford, Rachael. N. Slaybaugh, and Kevin. T. Clarno, "Denovo: A New Three-Dimensional Parallel Discrete Ordinates Code in SCALE," *Nuclear Technology* **171**(2), 171-200 (2010).

Faissol, Daniel M., Kevin.Ni, David J. Lange, Karl E. Nelson, Claudio P. Santiago, Thomas A. Edmunds, Padmini R. Sokkappa and Richard M. Wheeler, "Modeling and Simulation to Guide Radiological and Nuclear Search Tactics, Techniques and Procedures," LLNL-TR-596992, Lawrence Livermore National Laboratory, Livermore, California, October 2012.

Gardner, Robin P. and Avneet Sood, "A Monte Carlo simulation approach for generating NaI detector response function (DRFs) that accounts for non-linearity and variable flat continua," *Nuclear Instruments and Methods in Physics Research B* **213**, 87-99 (2004).

Haghighat, Alireza and John C. Wagner, "Monte Carlo Variance Reduction with Deterministic Importance Functions," *Progress in Nuclear Energy* **42**(1), 25-53 (2003).

McConn, Ronald J. Jr., Christopher J. Gesh, Richard T. Pagh, Robert A. Rucker, and Robert G. Williams III, "Compendium of Material Composition Data for Radiation Transport Modeling," PNNL-15870, Rev. 1, Pacific Northwest National Laboratory, Richland, Washington, March 2011.

Mitchell, Dean J., "Gamma Detector Response and Analysis Software (GADRAS)," Sandia National Laboratories, SAND88-2519, (1988).

Mitchell, Dean J., Lee T. Harding, Gregory G. Thoreson, and Steven M. Horne, "GADRAS Detector Response Function," SAND2014-1946, Sandia National Laboratories, Albuquerque, New Mexico, November 2014.

Peplow, Douglas E. "Monte Carlo Shielding Analysis Capabilities with MAVRIC," *Nuclear Technology* **174**(2), 289-313 (2011).

Rajpoot, Harish Chandra, *Advanced Geometry: Mathematical Analysis of Unified Articles*, Notion Press, Chennai, India, 2014 (ISBN: 9789383808151)

Wagner, John C. and Alireza Haghighat, "Automated Variance Reduction of Monte Carlo Shielding Calculations Using the Discrete Ordinates Adjoint Function," *Nuclear Science and Engineering* **128**, 186 (1998).

Wagner, John C., Douglas E. Peplow, and Scott W. Mosher, "FW-CADIS Method for Global and Semi-Global Variance Reduction of Monte Carlo Radiation Transport Calculations," *Nuclear Science and Engineering* **176**, No. 1, 37-57 (2014).

X-5 Monte Carlo Team, *MCNP—A General Monte Carlo N-Particle Transport Code, Version 5. Volume I: Overview and Theory*. LA-UR-03-1987. Los Alamos National Laboratory, Los Alamos, NM, 2003.